

Antiferromagnetic \mathbb{Z}_2 topological metal near the metal-insulator transition in MnS_2

Vsevolod Ivanov,^{1,2} Xiangang Wan,³ and Sergey Y. Savrasov⁴

¹*Virginia Tech National Security Institute, Blacksburg, Virginia 24060, USA*

²*Department of Physics, Virginia Tech, Blacksburg, Virginia 24061, USA*

³*National Laboratory of Solid State Microstructures,*

School of Physics and Collaborative Innovation Center of Advanced Microstructures, Nanjing University, Nanjing, China

⁴*Department of Physics, University of California, Davis, CA 95616, USA*

Antiferromagnetic (AFM) semiconductor MnS_2 possesses both high-spin and low-spin magnetic phases that can be reversibly switched by applying pressure. With increasing pressure, the high-spin state undergoes pressure-induced metalization before transforming into a low-spin configuration, which is then closely followed by a volume collapse and structural transition. We show that the pressure driven band inversion is in fact topological, resulting in an antiferromagnetic \mathbb{Z}_2 topological metal (Z2AFTM) phase with a small gap and a Weyl metal phase at higher pressures, both of which precede the spin-state crossover and volume collapse. In the Z2AFTM phase, the magnetic order results in a doubling of the periodic unit cell, and the resulting folding of the Brillouin zone leads to a \mathbb{Z}_2 topological invariant protected by the persisting combined time-reversal and half-translation symmetries. Such a topological phase was proposed theoretically by Mong, Essin, and Moore in 2010 for a system with AFM order on a face-centered cubic (FCC) lattice, which until now has not been found in the pool of real materials. MnS_2 represents a realization of this original proposal through AFM order on the Mn FCC sublattice. A rich phase diagram of topological and magnetic phases tunable by pressure, establishes MnS_2 as a candidate material for exploring magnetic topological phase transitions and for potential applications in AFM spintronics.

I. INTRODUCTION.

Non-magnetic topological materials have been extensively explored and classified in readily accessible materials databases [1–3], however, magnetic topological materials are comparatively less studied [4, 5]. In fact there are few examples of magnetic topological insulators, most of which are based on the $\text{Bi}_2\text{Se}/\text{Te}_3$ family of materials [6] into which magnetism is introduced by doping [7], a magnetic substrate [8], or through a heterostructure [9–11]. New materials hosting these kinds of phases can serve as platforms for studying the complex interplay between magnetism and topology, as well as transitions between different topological phases. In particular, the discovery of new antiferromagnetic (AFM) topological materials, is motivated by their potential applications in the field of AFM spintronics [12, 13].

The earliest example of an antiferromagnetic topological insulator (AFTI) [14] was theoretically proposed shortly after the experimental discovery of the first topological insulator. In this model AFTI, time reversal symmetry Θ is broken by antiferromagnetism, leading to a doubling of the periodic unit cell. However, the combination of time-reversal and half-translation symmetries of this new unit cell, $\Theta T_{1/2}$, is preserved, and leads to a \mathbb{Z}_2 invariant classifying the AFM topological phases. In the AFTI, the \mathbb{Z}_2 parameters of the undoubled cell, γ_0 and γ_π , which correspond to the $k_z = 0, \pi$ time reversal invariant planes, combine together when Brillouin zone is folded in half to make these $k_z = 0$ and $k_z = \pi$ planes coincide. The resulting new \mathbb{Z}_2 coefficient of the doubled cell is equal to $\gamma_0^d = \gamma_0 + \gamma_\pi = s$, which can take on a value of 0 or 1 depending on if the system is

a trivial ($s = 0$) or topologically protected ($= 1$) phase. This type of $\Theta T_{1/2}$ -symmetry protected AFTI phase was recently confirmed in MnBi_2Te_4 [9], but a realization of the originally proposed AFTI arising from AFM ordering on a face centered cubic (FCC) sublattice has yet to be discovered.

The series of first-row transition metal dichalcogenides with the pyrite structure display a range of electronic phases depending on the electron filling. The crystal field environment of the tilted sulfur octahedra around each transition metal atom results in the splitting of the $3d$ manifold into a lower t_{2g} band and an upper e_g band. ZnS_2 , which has a $3d^{10}$ electronic configuration is a paramagnetic insulator [15]. Moving down the series, CuS_2 ($3d^9$) is a superconductor [16], NiS_2 ($3d^8$) is an antiferromagnetic Mott insulator [17–19], CoS_2 ($3d^7$) is a ferromagnetic Weyl metal [20, 21], and FeS_2 ($3d^6$) becomes a small gap semiconductor due to a completely empty e_g band [22, 23].

The $3d^5$ electron configuration of MnS_2 results in an interesting deviation from the expected trend in material properties determined by the electronic filling in this series. The increased stability of a half-occupied $3d$ orbital leads to a competition between high-spin and low-spin states. Energetic proximity of these states leads to a pressure driven magnetic transition which is accompanied by a structural transformation and volume collapse.

In this work, we show that the complex electronic structure of MnS_2 under pressure is further enriched by a series of topological phases. Using first-principles electronic structure calculations we show that the recently discovered pressure-induced metalization in this material occurs due to a crossing of the antibonding $S_2^- 3p-\sigma^*$ and

Mn $3d$ - e_g bands at the Γ point. The spin-orbit coupling creates a small indirect gap in this crossing, which we show is in fact a Z2AFTM phase, by performing a parity analysis and direct calculations of the \mathbb{Z}_2 topological invariant. The AFM ordering of the face centered cubic (FCC) Mn sublattice, thus makes this a realization of the original proposal of the 3D AFTI protected by $\Theta T_{1/2}$ symmetry [14]. Further compression of the lattice results in a metallic Weyl phase [24]. Both topological phases would exhibit an anomalous Hall effect; semi-quantized for the Weyl phase, and quantized for the Z2AFTM.

II. STRUCTURE AND MAGNETISM.

MnS_2 crystallizes in the cubic $Pa\bar{3}$ space group (#205) at ambient pressure (Figure 1a). The sulfur atoms in the structure form covalently bonded dimers that behave effectively as single S_2^{2-} units linking together the tilted MnS_6 octahedral clusters. The FCC sub-lattice of Mn moments arranges in the AFM-III type magnetic ordering below 48.2 K, doubling the cubic unit cell [25]. This magnetic transition temperature increases with pressure, reaching 76K at 5.3 GPa [26].

At ambient pressure, the system is insulating with the d -band of Mn split into spin-up and spin-down, the lower of which is fully occupied, yielding an $S = 5/2$ high spin

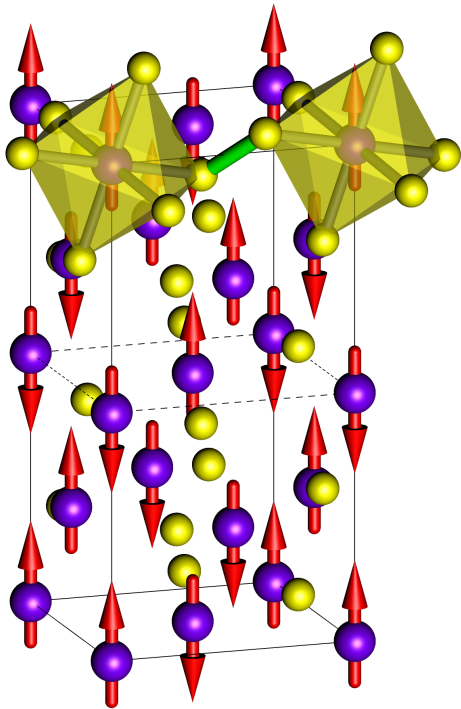


FIG. 1. Crystal structure of the magnetic unit cell of MnS_2 . Manganese atoms (purple) form an FCC sublattice, and sulfur atoms (yellow) surround each Mn atom in an octahedral arrangement. Arrows indicate the magnetic moments on the Mn atoms in the AFM-III phase below $T_N = 48\text{K}$.

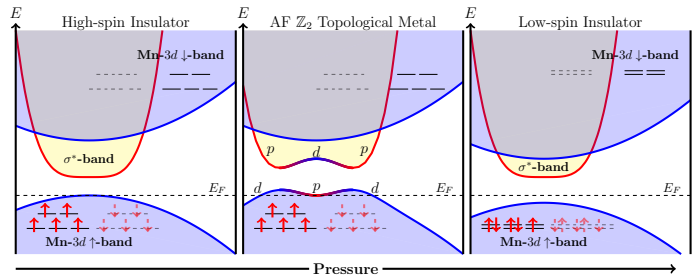


FIG. 2. Schematic of the band-structure of MnS_2 at ambient pressure (left), near the insulator-to-metal transition (middle,) and high pressure (right). Dashed and solid lines/arrows correspond to states/electrons on opposite spin Mn sites.

state. The conduction band also has contributions from the S_2^{2-} dimers, where the p -orbitals on S form an antibonded orbital $3p\text{-}\sigma^* = (p - p')/\sqrt{2}$. Upon applying pressure, the crystal field splitting between the t_{2g} and e_g bands increases (Figure 2), resulting in all of the electrons occupying the t_{2g} band, forming an $S = 1/2$ low-spin state. The transition into the low-spin state is accompanied by a structural transition to the arsenopyrite structure at $\sim 11\text{GPa}$, and a colossal volume collapse of 22% – the largest reversible volume collapse currently known[27]. The high-pressure structure with the low-spin state persists under decompression up to 6GPa before reverting back to the nominal pyrite structure. It was recently shown that the electronic transformation to the low-spin state under increasing pressure precedes and may in fact drive the structural transformation [28].

Both the high-spin and low-spin phases show characteristics of Mott insulators [29, 30], though more recent work has concluded that the material is in fact a charge transfer insulator [27]. Pressure dependent conductivity measurements revealed a metal-insulator-transition (MIT), marked by an eight order-of-magnitude increase in conductivity just before the spin-state crossover [27].

To model the electronic structure of MnS_2 across the magnetic transition under pressure, the compressed structures were first relaxed using the full potential linearized augmented plane wave (FLAPW) method as implemented in WIEN2K [31], starting from the experimental pyrite structure. The structural relaxations were performed using a LDA+SO+ U approach, with spin-orbit coupling, and Coulomb interactions were taken into account in the self-interaction correction (SIC) approximation [32].

To ensure that our conclusions are not dependent on the parameters of the LDA+SO+ U method, we perform our calculations with both $U = 4\text{eV}$ and $U = 5\text{eV}$, and a value of $J = 1\text{eV}$ for the Hund's coupling. For the experimental lattice parameters at ambient pressure, our calculation reproduces the experimentally observed AFM Type-III ordering of the magnetic moments, consistent with prior simulations of this material [28]. The computed magnetic moment on the Mn atoms is $4.42\mu_B$

for $U = 4\text{eV}$, while for $U = 5\text{eV}$ it increases slightly to $4.47\mu_B$. These values are consistent with a high-spin $S = 5/2$ state.

Both the $U = 4\text{eV}$ and $U = 5\text{eV}$ cases are semiconductors at ambient pressure, with relatively large gaps of 1.23eV and 1.40eV respectively. As the pressure is increased, the highest occupied Mn $3d - e_g$ bands are pushed upward in energy due to increasing crystal field interactions, bringing them closer to the unoccupied $S_2\sigma^*$ band just above E_F , leading to a narrowing of the gap. Under sufficiently high compression of the lattice the valence and conduction bands cross, leading to a metallic state, before the material reverts back to an insulating state at even higher pressures. The compression also suppresses the magnetic moment, which decreases rapidly after the onset of pressure induced metalization, and ultimately collapses into a low-spin state simultaneously with the reappearance of the electronic gap.

In order to more closely examine these various transitions under pressure, a wide range of lattice compressions was scanned to determine the region of interest for the metalization and suppression of the magnetic moment. The band crossing at E_F and subsequent transformation into the low-spin state was found to occur within a narrow range of 25% to 30% volume compression. The relaxed structures between 25% and 30% in increments of 1% were used to perform calculations using LDA+SO+ U within the full-potential muffin-tin orbital framework (FP-LMTO), to validate the FLAPW results and compute topological properties.

Under pressure, the relaxed structure of MnS_2 undergoes a number of changes as compared to the ideal uncompressed pyrite structure. The magnetic order breaks the cubic symmetry of the structure, reducing it to the orthorhombic magnetic space group P_bca2_1 . This means that during the structural relaxation, the atoms are free to move as long as they respect the orthorhombic symmetry, so the final atomic positions of the structure may break the cubic $Pa\bar{3}$ symmetry as well. Fig 3 shows

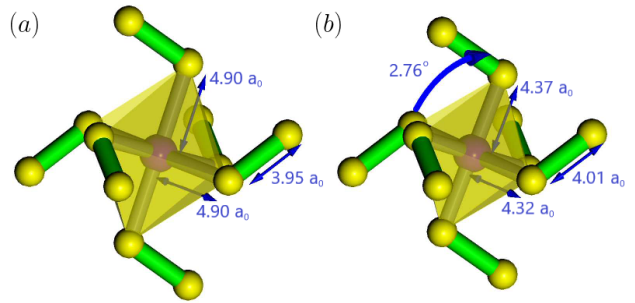


FIG. 3. Structure of the $\text{Mn}(\text{S}_2)_6$ octahedra for a), the ideal experimental uncompressed structure and b), the computed relaxed structure at 27% compression. Bond lengths in Bohr (a_0) are indicated, as well as the rotation of the main octahedron in degrees.

that as the structure is compressed, the octahedra rotate slightly by 2.76° , and are also significantly compressed. On the other hand, the sulfur dimers expand slightly despite the overall structural compression, and a Jahn-Teller-like distortion develops in the octahedra. All of these structural changes work in tandem to drive a band inversion under high pressure. The slightly differing lengths of the octahedral bonds break the degeneracy of both the Mn $3d-e_g$ bands below E_F , and the $S_2^{2-} 3p-\sigma^*$ bands above E_F , while the shortening of the bonds results in a greater overlap of the Mn and S_2^{2-} centered orbitals, reducing the size of the band gap. Furthermore, the lengthening of the S_2^{2-} dimers results in a lower energy for the antibonding $3p-\sigma^*$ orbital, forming an electron-like band around the Γ point which dips in energy below the rest of the manifold, and ultimately inverts with the hole-like Mn $3d-e_g$ band at higher pressures. To further understand how the band inversion and metalization is driven by the structural distortion, we compute the band structures at different compression levels while keeping the relative atomic positions fixed to those of the high-pressure end-state [33]. The band inversion occurs much earlier, at compressions as low as 20%, showing that the structural distortion in fact helps drive the band inversion. In experiments, the insulator-to-metal transition occurs at much lower pressures than predicted by theory, suggesting that this structural distortion may in fact already be present at lower pressures.

The computed magnetic moments for the compressed structures across the magnetic transition are shown in Table I. For the calculation with $U = 4\text{eV}$, the high spin state at 25% compression has a magnetic moment that is reduced slightly from theoretical ideal value for the $S = 5/2$ magnetism, yielding a value of $3.8\mu_B$. With pressure the moment decreases to $3.5\mu_B$ at 27% compression, where the bands first cross. Compressing beyond this volume results in a rapid reduction of the Mn magnetic moment to $1.2\mu_B$ at 30% compression, which is consistent with $S = 1/2$ magnetism. The calculations at $U = 5\text{eV}$ follow a similar trend, though the magnetic

Compression $1 - V/V_0$	$U = 4.0\text{eV}$		$U = 5.0\text{eV}$	
	$M(\mu_B)$	phase	$M(\mu_B)$	phase
0%	4.42	NI	4.47	NI
25%	3.80	NI	4.02	NI
26%	3.74	NI	3.97	NI
27%	3.51	Z2AFTM	3.92	NI
28%	2.98	WM	3.84	NI
29%	1.24	NI	3.73	Z2AFTM
30%	1.22	NI	2.59	WM

TABLE I. Mn magnetic moments for different compressions of the MnS_2 pyrite structure, for varying values of Hubbard U . The phase at each pressure is indicated as normal insulator (NI), weyl metal (WM), or anti-ferromagnetic \mathbb{Z}_2 topological metal (Z2AFTM).

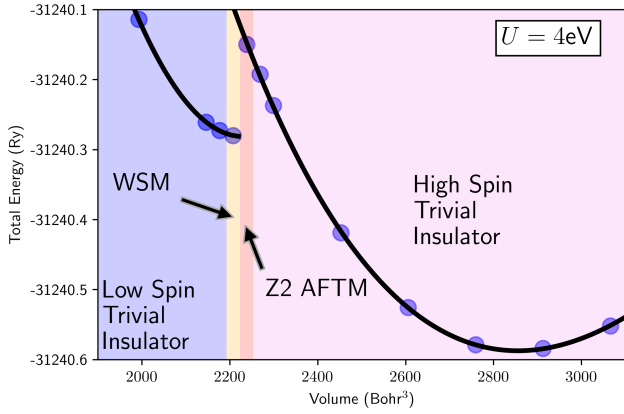


FIG. 4. Total energy of MnS_2 computed for different unit cell volumes for $U = 4\text{eV}$. The black lines is the Birch-Murnaghan equation of state fitted to the high-spin phase structures. Shaded panels denote the various phases occurring at different pressures: blue – low-spin trivial insulator, orange – WSM, red – AFTI, violet – high-spin trivial insulator.

moments are slightly larger, and a higher compression is needed in order to drive the transition into $S = 1/2$ magnetism. This change in the electronic structure is known to precede the collapse to the arsenopyrite structure [27, 28], thus at these higher pressures the ambient pyrite structure may no longer be the ground state.

The calculations at varying pressures were fitted to the Birch-Murnaghan [34] equation of state (Figure 4). The theoretical equation of state fits the computed energies of MnS_2 very well up to the point of metalization, but deviates significantly for higher compressions, consistent with a transition to a distinct electronic phase. The fit also allows us to extract the external pressure needed to stabilize each lattice volume. For the $U = 4\text{eV}$ calculation, an expansion pressure of -4.8 GPa is necessary, since computed equilibrium volume is in fact 2.3% smaller than the experimental value. On the other hand for $U = 5\text{eV}$, compression with a pressure of 4.0 GPa is needed, as the equilibrium volume is 1.7% larger. The insulator to metal transition takes place at a pressure of 23.8 GPa (27% compression) for $U = 4\text{eV}$, and 45.8 GPa (29% compression) for $U = 5\text{eV}$ (See Supplementary Material at [33]), compared to the experimental value of 11 GPa. Despite the quantitative disagreement with experiment, these simulations correctly reproduce the insulator-to-metal transition and concomitant suppression of the magnetic moment, and are consistent with prior calculations which placed the metalization around ~ 20 GPa [28].

The subsequent discussion will focus on the calculations with $U = 4\text{eV}$ due to the better quantitative agreement with the experimentally measured insulator to metal transition, though it should be noted that the results do not depend on the simulation parameters, with higher values of U simply requiring higher pressures to reproduce the same phases.

III. TOPOLOGY

We will now discuss the topological properties of MnS_2 . The parity criterion [35, 36] for identifying topologically nontrivial phases is valid in systems possessing inversion symmetries, as is the case for MnS_2 , and is therefore useful for understanding the origin of the topology. Ignoring the magnetism, at the time-reversal invariant Γ point the odd parity $S_2^- 3p-\sigma^*$ band crosses E_f , inverting with the lower-lying even parity Mn $3d-e_g$ band (Fig. 5). This band inversion is a strong indication of the presence of topological feature.

We now turn to the computational treatment of MnS_2 , focusing on the 25%, 26%, and 27% compressed structures. To verify the topological properties, special care must be taken to consider other possibilities that may arise. When either time reversal or inversion symmetries are broken, topological Weyl points [24] may arise in the electronic band structure. These Weyl points may be located at arbitrary points in the Brillouin zone, and might exist despite the apparent gap in the band structure when plotting along high symmetry lines. To check for the presence of Weyl points we use an approach which locates sources and sinks of Berry curvature [37]. This procedure computes an integer link field using the FP-LMTO electronic structure, eliminating the need for projecting onto Wannier orbitals. The search is carried out on a $20 \times 20 \times 10$ \mathbf{k} -point grid, and yields no topological point nodes for the 25-27% compression range.

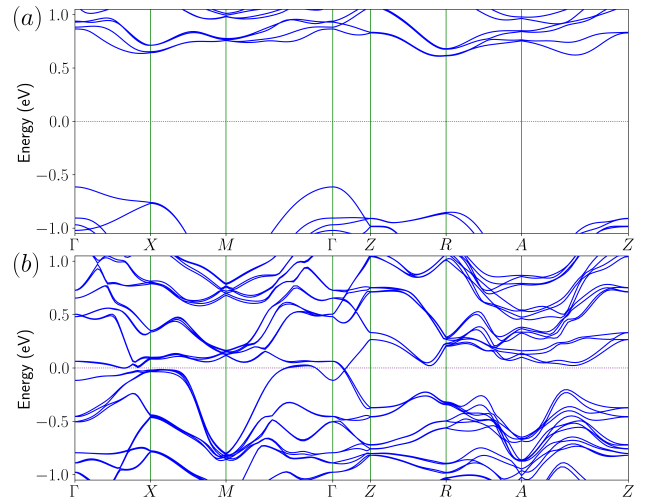


FIG. 5. Band structures of MnS_2 for (a) no compression and (b) 27% compression. In (b) the bands invert around the Γ point, and there is a gap throughout the Brillouin zone.

We now discuss the topological nature of the band gap in MnS_2 across the 25-27% compression range. In MnS_2 the magnetic ordering breaks time-reversal symmetry, doubling the unit cell. In effect, both time reversal symmetry Θ and half-translation symmetry $T_{1/2}$ are broken. In particular, the \mathbb{Z}_2 invariant of the $\mathbf{k}_z^d = 0$

plane in the BZ of the doubled cell, is exactly equal to the strong topological invariant, $\gamma_0^d = \gamma_0 + \gamma_\pi = s$, with $s = 1$ corresponding to the topologically nontrivial state. Thus computing the new \mathbb{Z}_2 invariant γ_0^d thus directly determines whether the material constitutes a topologically nontrivial phase as described by s .

The \mathbb{Z}_2 invariants for the structures in the 25-27% compression range are computed using the link variable method [38, 39]. This method is known to be quite stable, reproducing the integer topological invariants even for relatively coarse \mathbf{k} -point grids. To compute the invariants, we use 20 divisions of the Brillouin Zone to define the grid. The procedure uncovers a topologically trivial ($\gamma_0^d = s = 0$) phase at 25% compression, and topologically non-trivial ($\gamma_0^d = s = 1$) phase at 26% - 27% compression. It should be noted that while this confirms a topological insulator phase, at 27% compression there are bands crossing E_f , and at 26% the gap is ~ 10 meV, meaning the system is effectively metallic. Convergence of the \mathbb{Z}_2 invariant calculation was checked for \mathbf{k} -point grids up to 50×50 , confirming the existence of the topological transition.

The essential features of the Z2AFTM phase in MnS₂ can be captured using a simple tight binding model using a basis of a Mn-3d orbital and the σ^* orbital of the S₂ dimers, both of which lie on FCC sublattices, that taken together form a rock-salt type structure. The effective Hamiltonian can be written as

$$\mathcal{H} = \mathcal{H}_0 + \mathcal{H}_{d-\sigma^*} + \mathcal{H}_{\text{so}} + \mathcal{H}_{\text{mag}}. \quad (1)$$

The first term represents the onsite energies of the S₂- σ^* orbitals ($p_{i\alpha}^\dagger, p_{i\alpha}$), and Mn-3d orbitals ($d_{i\alpha}^\dagger, d_{i\alpha}$),

$$\mathcal{H}_0 = \epsilon_{\sigma^*} \sum_{i\alpha} p_{i\alpha}^\dagger p_{i\alpha} + \epsilon_d \sum_{i\alpha} d_{i\alpha}^\dagger d_{i\alpha}, \quad (2)$$

where i and α represent the site and spin indices respectively. The second term is comprised of the nearest neighbor and next-nearest neighbor hoppings between orbitals,

$$\begin{aligned} \mathcal{H}_{d-\sigma^*} = & \sum_{ij\alpha} \left[t_{\sigma^*} p_{i\alpha}^\dagger p_{j\alpha} + t_d d_{i\alpha}^\dagger d_{j\alpha} \right. \\ & \left. + t_{d\sigma^*} \left(d_{i\alpha}^\dagger p_{j\alpha} + p_{i\alpha}^\dagger d_{j\alpha} \right) \right]. \quad (3) \end{aligned}$$

The spin orbit couples between the non-magnetic orbitals,

$$\mathcal{H}_{\text{so}} = it_{\text{so}} \sum_{ij\alpha\alpha'} p_{i\alpha}^\dagger \boldsymbol{\sigma} \cdot (\mathbf{d}_{ij}^1 \times \mathbf{d}_{ij}^2) p_{j\alpha'}, \quad (4)$$

where $\boldsymbol{\sigma} = (\sigma_x, \sigma_y, \sigma_z)$ is the vector of Pauli matrices, and $\mathbf{d}_{ij}^1, \mathbf{d}_{ij}^2$ are the two nearest neighbor bond vectors that are traversed between the second-nearest neighbor sites i and j . In particular, this term is only non-zero when the two intermediate Mn sites have equal magnetization, otherwise the cross products ($\mathbf{d}_{ij}^1 \times \mathbf{d}_{ij}^2$), will cancel [14]. Finally, antiferromagnetic order is introduced

Position	$E - E_F$ (meV)	Chirality
(0.2126, 0.3325, 0.0413)	-287 meV	-1
(0.1896, 0.4140, 0.2747)	-283 meV	-1
(0.2891, 0.1111, 0.4618)	-54 meV	-1
(0.3487, 0.1251, 0.0609)	-131 meV	-1
(0.2092, 0.4024, 0.2420)	-61 meV	-1
(0.3917, 0.0507, 0.0340)	+129 meV	+1

TABLE II. The k -space locations in units of $(2\pi/a, 2\pi/a, 2\pi/a)$, energy relative to E_F , and chirality of the symmetry-inequivalent Weyl points in the Weyl metal phase of MnS₂.

through the term $\mathcal{H}_{\text{mag}} = \lambda s_i \sigma_z$, where $s_i = +1$ or -1 for spin up or spin down Mn atoms, and σ_z is the Pauli matrix acting on the electron spin degree of freedom.

In order to qualitatively reproduce the \mathbb{Z}_2 topological phase in MnS₂, we take the model parameters to be $\epsilon_d = -2.2$, $\epsilon_{\sigma^*} = 1.9$, $t_{\sigma^*} = -0.15$, $t_d = 0.2$, $t_{d\sigma^*} = 0.5$, and magnetic splitting $\lambda = 0.2$. As the spin-orbit coupling $0 < t_{\text{so}} < 0.3$ is increased, the valence band maximum and conduction band minimum invert at the gamma point. It should be noted that in the real material, the spin-orbit coupling will be much smaller than the hopping $t_{\text{so}} \ll t_{d\sigma^*}$. In the model, the same physics can be recovered with a much smaller t_{so} if the gap is decreased by lowering ϵ_{σ^*} , however, we choose a larger value in order to more clearly visualize the surface states. A 10-layer slab calculation reveals that when the bands are inverted by spin-orbit coupling, a single Dirac cone appears on the z -surface, protected by the combined time-reversal and half-translation symmetries. The exact form of the Hamiltonian used is provided in the supplementary material [33], along with details on the slab calculations of the topological surface states.

Continuing to 28% compression of the lattice results in a metallic Weyl phase, for which the previously described Weyl point search procedure [37] yields a number of symmetry protected Weyl points in the Brillouin zone between the two bands crossing at E_F . The cubic lattice symmetry of MnS₂ is broken by AFM order in the z direction, so the Weyl points generate in symmetry-related sets of eight at the positions given in Table II. Each listed Weyl has symmetry-related members found at $(\pm k_x, \pm k_y, \pm k_z)$, with Weyl points related by a reflection having opposite chirality.

Both the Weyl metal and Z2AFTM phases should exhibit an anomalous Hall effect (AHE) [14, 40] that can be observed experimentally to detect the onset of these topological phases under pressure. In the Z2AFTM phase, the surface of MnS₂ would have a 2D half-quantized AHE $\sigma_{xy}^{2D} = e^2/(2h)$. In the Weyl metal phase, this exact quantization would break, due to the presence of Weyl points. Instead, each pair of Weyls would have a contribution [41] $\sigma_{xy}^{3D} = e^2 k_W / (2\pi h)$ to the 3D AHE, where k_z is the separation in k -space between the Weyl points

comprising the pair.

IV. CONCLUSION

Our prediction of Z2AFTM and Weyl metal phases within the spin-state crossover transition in MnS_2 , along with the recent confirmation of a Weyl semimetal phase in CoS_2 , has now cemented topology as yet another functional property of pyrite-type transition metal disulfides which already included strongly correlated Mott physics, superconductivity, and gate-induced magnetism. These results further reinforce the status of these transition metal disulfides as multifunctional materials for experimentally realizing a diverse range of exotic electronic properties.

The Z2AFTM phase in MnS_2 and Weyl semimetal phase in CoS_2 also motivate the search for topological phases in other pyrite-type TMDCs, which may be magnetic at higher temperatures or wider gaps due to stronger spin-orbit coupling from heavier elements. One such material is MnTe_2 [42], which orders antiferromagnetically at 86.5K, and also undergoes a pressure induced insulator-metal transition. Another possibility is the Mott insulator NiS_2 , which has AFM order below 40K [17–19], and can be made metallic either by applying moderate pressure or doping with Se at ambient pressure. If the topological phases were to exist, these materials would have much more suitable properties for applications such as AFM spintronics.

ACKNOWLEDGEMENTS

- [1] T. Zhang, Y. Jiang, Z. Song, H. Huang, Y. He, Z. Fang, H. Weng, and C. Fang, Catalogue of topological electronic materials, *Nature* **566**, 475 (2019).
- [2] M. G. Vergniory, L. Elcoro, C. Felser, N. Regnault, B. A. Bernevig, and Z. Wang, A complete catalogue of high-quality topological materials, *Nature* **566**, 480 (2019).
- [3] F. Tang, H. C. Po, A. Vishwanath, and X. Wan, Comprehensive search for topological materials using symmetry indicators, *Nature* **566**, 486 (2019).
- [4] N. C. Frey, M. K. Horton, J. M. Munro, S. M. Griffin, K. A. Persson, and V. B. Shenoy, High-throughput search for magnetic and topological order in transition metal oxides, *Science Advances* **6**, eabd1076 (2020), <https://www.science.org/doi/pdf/10.1126/sciadv.abd1076>.
- [5] Y. Xu, L. Elcoro, Z.-D. Song, B. J. Wieder, M. G. Vergniory, N. Regnault, Y. Chen, C. Felser, and B. A. Bernevig, High-throughput calculations of magnetic topological materials, *Nature* **586**, 702 (2020).
- [6] H. Zhang, C.-X. Liu, X.-L. Qi, X. Dai, Z. Fang, and S.-C. Zhang, Topological insulators in bi_2se_3 , bi_2te_3 and sb_2te_3 with a single dirac cone on the surface, *Nature Physics* **5**, 438 (2009).
- [7] C.-Z. Chang, J. Zhang, X. Feng, J. Shen, Z. Zhang, M. Guo, K. Li, Y. Ou, P. Wei, L.-L. Wang, Z.-Q. Ji, Y. Feng, S. Ji, X. Chen, J. Jia, X. Dai, Z. Fang, S.-C. Zhang, K. He, Y. Wang, L. Lu, X.-C. Ma, and Q.-K. Xue, Experimental observation of the quantum anomalous hall effect in a magnetic topological insulator, *Science* **340**, 167 (2013), <https://www.science.org/doi/pdf/10.1126/science.1234414>.
- [8] S. Eremeev, V. Menshov, V. Tugushev, and E. Chulkov, Interface induced states at the boundary between a 3d topological insulator bi_2se_3 and a ferromagnetic insulator eu_s , *Journal of Magnetism and Magnetic Materials* **383**, 30 (2015), selected papers from the sixth Moscow International Symposium on Magnetism (MISM-2014).
- [9] M. M. Otrokov, I. I. Klimovskikh, H. Bentmann, D. Estyunin, A. Zeugner, Z. S. Aliev, S. Gaß, A. U. B. Wolter, A. V. Koroleva, A. M. Shikin, M. Blanco-Rey, M. Hoffmann, I. P. Rusinov, A. Y. Vyazovskaya, S. V. Eremeev, Y. M. Koroteev, V. M. Kuznetsov, F. Freyse, J. Sánchez-Barriga, I. R. Amiraslanov, M. B. Babanly, N. T. Mamedov, N. A. Abdullayev, V. N. Zverev, A. Alfonsov, V. Kataev, B. Büchner, E. F. Schwier, S. Kumar, A. Kimura, L. Petaccia, G. Di Santo, R. C. Vidal, S. Schatz, K. Kißner, M. Ünzelmann, C. H. Min, S. Moser, T. R. F. Peixoto, F. Reinert, A. Ernst, P. M. Echenique, A. Isaeva, and E. V. Chulkov, Prediction and observation of an antiferromagnetic topological insulator, *Nature* **576**, 416 (2019).
- [10] R. C. Vidal, A. Zeugner, J. I. Facio, R. Ray, M. H. Haghighi, A. U. B. Wolter, L. T. Corredor Bohorquez, F. Cagliaris, S. Moser, T. Figgemeier, T. R. F. Peixoto, H. B. Vasili, M. Valvidares, S. Jung, C. Cacho, A. Alfonsov, K. Mehlawat, V. Kataev, C. Hess, M. Richter, B. Büchner, J. van den Brink, M. Ruck, F. Reinert, H. Bentmann, and A. Isaeva, Topological electronic structure and intrinsic magnetization in mbi_4te_7 : A bi_2te_3 derivative with a periodic mn sublattice, *Phys. Rev. X* **9**, 041065 (2019).
- [11] K. He, Mnbi_2te_4 -family intrinsic magnetic topological materials, *npj Quantum Materials* **5**, 90 (2020).
- [12] T. Jungwirth, X. Marti, P. Wadley, and J. Wunderlich, Antiferromagnetic spintronics, *Nat. Nanotechnol.* **11**, 231 (2016).
- [13] C. Niu, H. Wang, N. Mao, B. Huang, Y. Mokrousov, and Y. Dai, Antiferromagnetic topological insulator with nonsymmorphic protection in two dimensions, *Phys. Rev. Lett.* **124**, 066401 (2020).
- [14] R. S. K. Mong, A. M. Essin, and J. E. Moore, Antiferromagnetic topological insulators, *Phys. Rev. B* **81**, 245209 (2010).
- [15] T. A. Bither, R. J. Bouchard, W. H. Cloud, P. C. Donohue, and W. J. Siemons, Transition metal pyrite dichalcogenides. high-pressure synthesis and correlation of properties, *Inorganic Chemistry* **7**, 2208 (1968).
- [16] Y. Takano, N. Uchiyama, S. Ogawa, N. Môri, Y. Kimishima, S. Arisawa, A. Ishii, T. Hatano, and K. Togano, Superconducting properties of $\text{cus}_2\text{-xsex}$ under high pressure, *Physica C: Superconductivity* **341-348**, 739 (2000).
- [17] A. Y. Matsuura, Z. X. Shen, D. S. Dessau, C. H. Park, T. Thio, J. W. Bennett, and O. Jepsen, Electronic structure and the metal-insulator transition in $\text{NiS}_{2-x}\text{Se}_x$,

- Phys. Rev. B* **53**, R7584 (1996).
- [18] A. Y. Matsuura, H. Watanabe, C. Kim, S. Doniach, Z.-X. Shen, T. Thio, and J. W. Bennett, Metal-insulator transition in $\text{NiS}_{2-x}\text{Se}_x$ and the local impurity self-consistent approximation model, *Phys. Rev. B* **58**, 3690 (1998).
- [19] D. D. Sarma, S. R. Krishnakumar, E. Weschke, C. Schüßler-Langeheine, C. Mazumdar, L. Kilian, G. Kaindl, K. Mamiya, S.-I. Fujimori, A. Fujimori, and T. Miyadai, Metal-insulator crossover behavior at the surface of NiS_2 , *Phys. Rev. B* **67**, 155112 (2003).
- [20] C. Leighton, M. Manno, A. Cady, J. W. Freeland, L. Wang, K. Umemoto, R. M. Wentzcovitch, T. Y. Chen, C. L. Chien, P. L. Kuhns, M. J. R. Hoch, A. P. Reyes, W. G. Moulton, E. D. Dahlberg, J. Checkelsky, and J. Eckert, Composition controlled spin polarization in $\text{Co}_{1-x}\text{Fe}_x\text{S}_2$ alloys, *Journal of Physics: Condensed Matter* **19**, 315219 (2007).
- [21] N. B. M. Schröter, I. Robredo, S. Klemenz, R. J. Kirby, J. A. Krieger, D. Pei, T. Yu, S. Stolz, T. Schmitt, P. Dudin, T. K. Kim, C. Cacho, A. Schnyder, A. Bergara, V. N. Strocov, F. de Juan, M. G. Vergniory, and L. M. Schoop, Weyl fermions, fermi arcs, and minority-spin carriers in ferromagnetic CoS_2 , *Science Advances* **6**, eabd5000 (2020), <https://www.science.org/doi/pdf/10.1126/sciadv.abd5000>.
- [22] E. H. Nickel, D. J. Vaughan, J. R. Craig, *Mineral Chemistry of Metal Sulfides*. (Cambridge Earth Science Series), Cambridge (Cambridge University Press), 1978. xvi+493pp., 167 figs. price £19.50., *Mineralogical Magazine* **43**, 186–187 (1979).
- [23] J. Walter, B. Voigt, E. Day-Roberts, K. Heltemes, R. M. Fernandes, T. Birol, and C. Leighton, Voltage-induced ferromagnetism in a diamagnet, *Science Advances* **6**, eabb7721 (2020), <https://www.science.org/doi/pdf/10.1126/sciadv.abb7721>.
- [24] X. Wan, A. M. Turner, A. Vishwanath, and S. Y. Savrasov, Topological semimetal and fermi-arc surface states in the electronic structure of pyrochlore iridates, *Phys. Rev. B* **83**, 205101 (2011).
- [25] L. M. Corliss, N. Elliott, and J. M. Hastings, Antiferromagnetic structures of mns_2 , mnse_2 , and mnte_2 , *Journal of Applied Physics* **29**, 391 (1958), <https://doi.org/10.1063/1.1723149>.
- [26] V. A. Sidorov, J. Guo, L. Sun, and V. V. Brazhkin, Thermodynamics of a magnetic transition in mns_2 at high pressures, *JETP Letters* **107**, 311 (2018).
- [27] S. A. J. Kimber, A. Salamat, S. R. Evans, H. O. Jeschke, K. Muthukumar, M. Tomić, F. Salvat-Pujol, R. Valentí, M. V. Kaisheva, I. Zizak, and T. Chatterji, Giant pressure-induced volume collapse in the pyrite mineral mns_2 , *Proceedings of the National Academy of Sciences* **111**, 5106 (2014), <https://www.pnas.org/content/111/14/5106.full.pdf>.
- [28] D. Durkee, D. Smith, R. Torchio, S. Petitgirard, R. Briggs, I. Kantor, S. R. Evans, T. Chatterji, T. Irifune, S. Pascarelli, K. V. Lawler, A. Salamat, and S. A. Kimber, Electronic origins of the giant volume collapse in the pyrite mineral mns_2 , *Journal of Solid State Chemistry* **269**, 540 (2019).
- [29] A. Rohrbach, J. Hafner, and G. Kresse, Electronic correlation effects in transition-metal sulfides, *Journal of Physics: Condensed Matter* **15**, 979 (2003).
- [30] T. Chattopadhyay, T. Brückel, and P. Burlet, Spin correlation in the frustrated antiferromagnet mns_2 above the Néel temperature, *Phys. Rev. B* **44**, 7394 (1991).
- [31] P. Blaha, K. Schwarz, F. Tran, R. Laskowski, G. K. H. Madsen, and L. D. Marks, Wien2k: An apw+lo program for calculating the properties of solids, *The Journal of Chemical Physics* **152**, 074101 (2020), <https://doi.org/10.1063/1.5143061>.
- [32] V. I. Anisimov, I. V. Solov'ev, M. A. Korotin, M. T. Czyżyk, and G. A. Sawatzky, Density-functional theory and nio photoemission spectra, *Phys. Rev. B* **48**, 16929 (1993).
- [33] The Supplemental Material at [URL will be inserted by publisher] contains further details the tight-binding model and electronic structure calculations.
- [34] F. Birch, Finite elastic strain of cubic crystals, *Phys. Rev.* **71**, 809 (1947).
- [35] L. Fu and C. L. Kane, Topological insulators with inversion symmetry, *Phys. Rev. B* **76**, 045302 (2007).
- [36] A. M. Turner, Y. Zhang, R. S. K. Mong, and A. Vishwanath, Quantized response and topology of magnetic insulators with inversion symmetry, *Phys. Rev. B* **85**, 165120 (2012).
- [37] V. Ivanov and S. Y. Savrasov, Monopole mining method for high-throughput screening for weyl semimetals, *Phys. Rev. B* **99**, 125124 (2019).
- [38] T. Fukui and Y. Hatsugai, Quantum spin hall effect in three dimensional materials: Lattice computation of \mathbb{Z}_2 topological invariants and its application to Bi_2 and Sb_2 , *Journal of the Physical Society of Japan* **76**, 053702 (2007), <https://doi.org/10.1143/JPSJ.76.053702>.
- [39] W. Feng, J. Wen, J. Zhou, D. Xiao, and Y. Yao, First-principles calculation of \mathbb{Z}_2 topological invariants within the fp-lapw formalism, *Computer Physics Communications* **183**, 1849 (2012).
- [40] A. A. Burkov, Anomalous hall effect in weyl metals, *Phys. Rev. Lett.* **113**, 187202 (2014).
- [41] K.-Y. Yang, Y.-M. Lu, and Y. Ran, Quantum hall effects in a weyl semimetal: Possible application in pyrochlore iridates, *Phys. Rev. B* **84**, 075129 (2011).
- [42] P. Vulliet, J. P. Sanchez, D. Braithwaite, M. Amanowicz, and B. Malaman, Pressure-induced metallization and collapse of the antiferromagnetic state of mnte_2 , *Phys. Rev. B* **63**, 184403 (2001).